Nanoscale

Tuning Two-dimensional Phase Formation Through Epitaxial Strain and Growth Conditions: Silica and Silicate on Ni_xPd_{1-x} (111) Alloy Substrates

Journal:	*Nanoscale*
Manuscript ID	NR-ART-07-2019-005944.R2
Article Type:	Paper
Date Submitted by the Author:	20-Oct-2019

Complete List of Authors:	Jhang, Jin-Hao; Yale University, Department of Chemical and Environmental Engineering Zhou, Chao; Yale University, Department of Mechanical Engineering and Materials Science Liang, Xin; Yale University, Department of Applied Physics Hutchings, Gregory; Yale University, Chemical and Environmental Engineering Fishman, Zachary; Yale University, Chemical Engineering Wu, Rongting; Yale University, Energy Sciences Institute Gozar, Adrian; Yale University, Energy Sciences Institute Schwarz, Udo; Yale University Ismail-Beigi, Sohrab; Yale University, Applied Physics Altman, Eric; Yale University, Department of Chemical and Environmental Engineering

Tuning Two-Dimensional Phase Formation Through Epitaxial Strain and Growth Conditions: Silica and Silicate on $Ni_xPd_{1-x}(111)$ Alloy Substrates

*Chao Zhou[1], *Xin Liang[2], Gregory S. Hutchings[3], Jin-Hao Jhang[3], Zachary S. Fishman[3], Rongting Wu[2,4], Adrian Gozar[2,4], Udo D. Schwarz[1,3], Sohrab Ismail-Beigi[1,2] and §Eric I. Altman[3]

[1]Department of Mechanical Engineering and Materials Science

[2]Department of Applied Physics

[3]Department of Chemical and Environmental Engineering

Yale University, New Haven, CT 06520 USA

[4]Energy Sciences Institute

Yale University, West Haven, CT 06516 USA

*Contributed equally.

§Corresponding author: eric.altman@yale.edu

Abstract

Two-dimensional (2D) materials can have multiple phases close in energy but with distinct properties, with the phases that form during growth dependent on experimental conditions and the growth substrate. Here, the competition between 2D van der Waals (VDW) silica and 2D Ni silicate phases on Ni_xPd_{1-x}(111) alloy substrates was systematically investigated experimentally as a function of Si surface coverage, annealing time and temperature, O_2 partial pressure, and substrate composition and the results were compared with thermodynamic predictions based on the DFT calculations and thermochemical data for O_2. Experimentally, 2D Ni silicate was exclusively observed at higher O_2 pressures (~10^{-6} Torr), higher annealing temperatures (1000 K), and more prolonged annealing (10 min) if the substrate contained any Ni and for initial Si coverages up to 2 monolayers. In contrast, decreasing the O_2 pressure to ~10^{-8} Torr and restricting the annealing temperature and time enabled 2D VDW silica formation. Amorphous 2D

VDW silica was observed even when the substrate composition was tuned to lattice match crystalline 2D VDW silica. The trend of decreased O_2 pressure favoring 2D VDW silica was consistent with the theoretical predictions; however, theory also suggested that sufficient Si coverage could avoid Ni silicate formation. The effect of epitaxial strain on 2D Ni silicate was investigated by modifying the solid solution alloy substrate composition. It was found that 2D Ni silicate will stretch to match the substrate lattice constant up to 1.12% tensile strain. When the lattice mismatch was over 1.40%, incommensurate crystalline domains were observed, indicating relaxation of the overlayer to its favored lattice constant. The limited epitaxial strain that could be applied was attributed to a combination of the 2D silicate stiffness, the insensitivity of its bonding to the substrate to its alignment with the substrate, and its lack of accessible structural rearrangements that can reduce the strain energy. The results demonstrate how the resulting 2D material can be manipulated through the growth conditions and how a solid solution alloy substrate can be used to maximize the epitaxial strain imparted to the 2D system.

Introduction

Two-dimensional (2D) van der Waals (VDW) heterostructures realized by stacking layers of 2D materials have attracted intense interest in recent years. Two popular methods are broadly employed to construct 2D VDW heterostructures. One is the direct mechanical assembly method involving delamination of individual layers followed by alignment and stacking of 2D layers.[1-3] The other is an epitaxial approach, which follows a bottom-up methodology and potentially yields larger 2D materials domains[4, 5] and fewer contaminants at the interfaces between layers.[6-8] A challenge with the epitaxial approach, however, is that the 2D layers of interest often exhibit multiple phases close in energy but with different properties.[9-11] Substrate interactions, lattice mismatch, and growth conditions all potentially play decisive roles in determining the phase that forms. In this work, the effect of growth conditions and epitaxial strain on the structure and formation of 2D silica and silicates on a series of Ni_xPd_{1-x}(111) substrates was systematically studied. It was found that adjusting the growth conditions allows selection between 2D VDW silica and 2D Ni silicate phases, and shown that the maximum epitaxial strain that can be imparted on the latter can be determined by varying the alloy substrate composition.

Epitaxial strain engineering has long been a tool to adjust the properties of three-dimensional (3D) materials.[12] While many 2D VDW materials also exhibit strain-dependent properties,[13-15]

using substrate lattice mismatch to apply the strain may be difficult because 2D materials interactions are often dominated by weak VDW forces. Thus, an important question is how much epitaxial strain can a substrate impart on a 2D material? The case of graphene as a canonical 2D VDW material is instructive to consider. Free-standing graphene layers display a six-membered ring structure with different-sized rings at domain boundaries.[16] Graphene layers grown on substrates show the same atomic structure; however, it is typically superimposed on top of a longer-range moiré pattern and the graphene lattice constant does not change by more than 1.2%.[17, 18] The moiré pattern is due to incommensuration between the graphene and the substrate, indicating that the graphene layer relaxes to its favored free-standing lattice constant and is not strained to match the substrate. Theoretical investigations of the impact of strain on graphene meanwhile predict that a Haeckelite structure composed of four- to eight-membered rings can become favored at large tensile strains, in the vicinity of 10%.[19, 20] Molecular dynamics simulations indicate that Haeckelite structures may also be trapped as metastable intermediates during graphene formation on metal substrates.[21] Since the ≈10% strain required to favor Haeckelite formation is well in excess of what can be applied through epitaxy, metastability would appear to be the only viable route to achieving non-ground state 2D carbon structures derived from graphene. On the other hand, the recently discovered 2D form of silica is predicted to have

experimentally accessible strain-induced phase transitions, making it an attractive system for inducing phase transitions and defects in honeycomb-structured 2D layers.[22, 23]

Two-dimensional VDW silica can be considered as an analog of graphene with SiO_4 tetrahedra replacing carbon atoms in the graphene structure.[24-28] The dangling bonds in a single plane of corner-sharing SiO_4 tetrahedra can be tied up by bonding to a metal substrate or through connections to a mirror-image plane of corner-sharing SiO_4 tetrahedra to form a 2D VDW bilayer.[29, 30] Similar to graphene, six-membered ring structures are favored; however, an amorphous phase composed of four- through nine-membered rings is also observed.[31-36] Consistent with experimental observations, theory indicates that structures incorporating different-sized rings are close in energy to the favored six-membered ring structure.[22, 34] Further, a modest 2.5% tensile strain is predicted to induce a phase transition to a structure incorporating four- and eight-membered rings.[22] Experimental results for single component metal surfaces are encouraging. On Ru(0001) with a tensile lattice mismatch of 2.1%, commensurate crystalline 2D VDW silica is observed together with an amorphous phase.[32] On Pt(111) with a 4.7% tensile mismatch, only the amorphous phase has been seen.[37] An incommensurate crystalline phase has been seen on Pd(111) with 3.8% tensile mismatch.[38] Meanwhile, on Pd(100) the growth is commensurate along [011] and incommensurate along $[01\bar{1}]$ with nearly regular defects observed

along the commensurate direction that were attributed to the 3.8% uniaxial strain.[39] Together the experimental results suggest that the substrate can impart the biaxial tensile strain close to what is needed to induce a phase transition, making 2D VDW silica an appealing system where phase transitions can be induced via strain by growth on metal alloy substrates. The recently developed Ni_xPd_{1-x}(111) epitaxial alloy system was chosen for this task because it forms a continuous solid solution with lattice constants that vary the strain from 6.0% compressive to 3.8% tensile.[40, 41] This paper targets the tensile regime because of the aforementioned prediction of 2D silica phase transitions under tensile strain.[22]

The above discussion focuses on the impact of the substrate lattice constant, but the chemical nature of the metal substrate and the growth conditions also play roles in determining the 2D structures that form. Prior results on pure metals highlight the relative strengths of Si–O and substrate metal–O bonds, as well as the Si coverage as key factors in determining the structures that form. For second and third row transition metals, Ru is at the dividing line for forming 2D VDW silica. When the amount of deposited silicon atoms is precisely controlled to form only one sheet of SiO_4 tetrahedra (i.e., half of a bilayer), a 2D monolayer structure can form on Ru(0001) that connects chemically to the substrate through Si–O–Ru linkages.[30] The amount of silicon in this case is denoted as 1 monolayer equivalent (MLE). When 2 MLE silicon atoms are deposited,

only the bilayer VDW structure can be detected. The monolayer and bilayer structures coexist when the coverage falls between 1 and 2 MLE; above 2 MLE, bulk 3D silica forms. To the left of Ru on the periodic table, only the 2D monolayer is seen on Mo, and Si deposition in excess of 1 MLE leads to 3D silica.[42-44] To the right of Ru, only the bilayer has been seen on Pd and Pt. The first row transition metals introduce the additional complication of the possibility of the formation of 2D silicates.[45, 46] When Fe and Ti were co-deposited with Si onto Ru(0001) and processed in oxygen, clay-like structures were observed in which a layer of six-membered rings of corner-sharing SiO_4 tetrahedra is stacked over a hexagonal layer of FeO_6 and TiO_6 octahedra; the octahedral sheet is connected to the alloy substrate through chemical bonds.[47-49] When 1 MLE Si was deposited onto an Ni_xPd_{1-x}(111) alloy substrate, Ni segregated to the interface and formed a 2D Ni silicate similar to the Fe and Ti silicates.[50]

Two-dimensional monolayer, bilayer, and Fe and Ti silicates are all formed through a high-temperature annealing process in oxygen. The quenching process is thought to influence the crystallinity of the overlayer. Both monolayer and bilayer silica show planar crystallinity when annealed in oxygen followed by slow cooling; however, amorphous bilayer silica has been observed under an increased cooling rate.[31, 32] The impact of the oxygen pressure during annealing can be intriguing to investigate for growth on Ni_xPd_{1-x}. While Ni is easier to oxidize than

Pd, it is more difficult to oxidize than Ti or Fe and thus it may be possible to find an oxygen chemical potential where silica remains stable but Ni does not oxidize, thereby making it possible to form 2D VDW silica.

In this paper, it will be shown that 2D VDW silica formation can be achieved on Ni_xPd_{1-x}(111) by limiting the oxygen pressure during the high temperature annealing step. Density functional theory (DFT) calculations together with thermochemical data for oxygen indicate that by varying the oxygen partial pressure and increasing the silicon supply, both 2D VDW silica and Ni silicate can be thermodynamically stable. For the Ni silicate, the structure was studied systematically as a function of alloy substrate composition and thus strain. A commensurate to incommensurate transition was observed between 1.12% and 1.40% tensile mismatch, experimentally pinpointing the maximum epitaxial strain that can be imparted to the 2D phase.

Methods

Experimental Methods

Following a previously reported recipe, 20 – 50 nm thick Ni_xPd_{1-x}(111) films were grown in ultra-high vacuum (UHV) by molecular beam epitaxy on 15 nm thick Cr_2O_3(0001) films grown on Al_2O_3(0001).[40] The lattice constants and thicknesses of the alloy films were determined by X-ray

diffraction and X-ray reflectivity data collected on a Rigaku SmartLab diffractometer. The alloy compositions were calculated from the measured lattice constants based on a quadratic approximation of Vegard's law.[40, 51]

Following growth, the Ni_xPd_{1-x}(111) films were transferred through air to another UHV system where silica-containing films were prepared and characterized. This UHV system was equipped with a double-pass cylindrical mirror analyzer for Auger electron spectroscopy (AES) measurements, reverse-view low energy electron diffraction (LEED) optics, and a high-speed variable temperature scanning tunneling microscope (STM).[52] The sample temperature was measured with a type-K thermocouple pressed against sample surface and was cross checked with a pyrometer.

After exposure to air, the Ni_xPd_{1-x}(111) films were cleaned by repeated cycles of Ar ion sputtering and post-annealing at 850 K in UHV until no surface contaminants were detectable by AES or LEED. The Si source for the films was SiO deposited onto the substrates at room temperature.[50] The SiO thickness and the oxygen pressure during deposition and during annealing were varied to target specific surface structures as detailed in the Results section.

Cut-and-pulled Pt/Ir tips were used for STM measurements. The tunneling current was set between 0.05 and 1.0 nA during scanning; no observable effects on the images were detected

over this current range. Polarization modulation reflection-absorption infrared spectroscopy (RAIRS) data were recorded in a dry nitrogen environment using a ThermoFisher Nicolet iS50 FTIR Spectrometer with the light incident at a grazing angle of 82°. LEED patterns at lower energies were recorded within an Elmitec LEEM-III low energy electron microscope. Our prior work has demonstrated that exposing silica-terminated Pd and Ni_xPd_{1-x} alloy samples to ambient conditions has no effect on the structure of the silica-containing layer.[39, 50]

Computational Methods

Density functional theory[53, 54] with the Perdew-Burke-Ernzerhof generalized gradient approximation (PBE GGA)[55] exchange-correlation functional was used for the computational work. Non-bonding interactions were taken into account using the DFT-D2 approach.[56] As detailed previously,[50] the calculations were performed using the Quantum Espresso software package with plane wave basis with an energy cutoff of 952.40 eV, periodic boundary conditions, and norm-conserving pseudopotentials.[57] Due to the metallic nature of the alloy substrates in our simulations, thermal smearing by 0.14 eV of the Kohn-Sham states' occupancies was employed together with a dense enough k point sampling of the Brillouin zone to achieve convergence. Various phases of silica and Ni silicate on the Ni-Pd(111) alloy

substrate were considered in the simulation. For monolayer and bilayer silica (2×2) surface unit cells and with $6 \times 6 \times 1$ k point grids were used, while Ni silicate was modeled using a $(2 \times 2\sqrt{3})$ surface unit cell and a $6 \times 4 \times 1$ k point grid. Because of the presence of Ni atoms in the simulation, spin polarization was also included in the electronic structure calculation. We compared results for the GGA combined with multiple VDW correction functionals (DFT-D2,[56] TS,[58] and VdW^{surf} [59]) for the SiO_2-on-metal system. The binding energies for SiO_2 produced from the three approaches were highly consistent and agreed with one another to within 0.1 eV/unit cell of each other, a magnitude much smaller than the chemical binding strength for silicate on metal surfaces. Therefore, the simplest DFT-D2 approach was chosen in our calculations which also has the advantage of treating the virtual atoms easily. The construction of the Ni_xPd_{1-x} alloy substrate using the virtual crystal approximation (VCA)[60] has been detailed in a prior publication.[50] Briefly, the substrate slabs contained one layer of Ni on top of four layers of VCA atoms with the bottom two layers fixed. Such a five layer thick slab has proven adequate to model 2D silica and transition metal silicates on metal surfaces.[29, 47] The computational parameters were sufficient to converge the total energy within 2 meV per atom. In the calculations, the slab systems were separated from their periodic images by at least 15 Å of vacuum to reduce artifacts introduced by slab-slab interactions. The structural relaxations were performed until all force components on all atoms were below 2.6×10^{-3} eV/Å (10^{-4} Ry/a_0 where a_0 is the Bohr radius).

Density functional theory calculations were carried out to understand the observed 2D silica/Ni silicate phase separation on Ni_xPd_{1-x}(111). As detailed below, a series of 2D silica and Ni silicate phases on $Ni_{0.5}Pd_{0.5}$(111) were studied.[50] The DFT calculations yielded the minimum energy structures for each phase at 0 K and zero oxygen partial pressure. Understanding and predicting the phases that form, however, requires theoretical methods that consider the experimental conditions. *First-principles atomistic thermodynamics* developed by Reuter and Scheffler was employed to tackle this task.[61] The method in the context of our study is briefly described below.

First-principles atomistic thermodynamics

The model slab can be considered to be in equilibrium with "reservoirs" of Si, O, and Ni with chemical potentials μ_i (i = Si, O, and Ni) that are defined by reference gas or bulk crystal phases. By allowing the slab to exchange atoms with the reservoirs at different chemical potentials, relative energies between phases can be compared at different experimental conditions (e.g. the temperature and oxygen partial pressure that determine the value of the oxygen chemical potential μ_O). The thermodynamically most stable 2D phase formed on the surface can be determined by the phase with the lowest surface free energy (per unit area) for the slab system, which is defined as

$$(1)\ \gamma(\{\mu_i\}) = \frac{1}{A}\left[G - \sum_i N_i\mu_i\right]$$

where G is the Gibbs free energy of the simulated slab. Since only the relative energies are of interest, N_i is taken as the excess number of atoms of the i^{th} species in the system relative to the clean $Ni_{0.5}Pd_{0.5}$ surface which is chosen as the baseline structure for comparison. As a result, the chemical potential term corresponding to the $Ni_{0.5}Pd_{0.5}$ virtual atoms in the bulk of the substrate drops out. The bottom surface of the slab was held fixed to the corresponding bulk configuration in the simulations, hence, the surface area A in equation (1) is equal to the area of one side of the surface unit cell. For example, for the clean $Ni_{0.5}Pd_{0.5}$ surface phase, $N_{Si} = N_O = N_{Ni} = 0$ in equation (1). Differences in the surface free energies of the phases were calculated with respect to the clean $Ni_{0.5}Pd_{0.5}$ surface which eliminated the influence of the bottom surface and alloy bulk. In defining the phase diagram for the system, regions of chemical potential μ_i (i = Si, O, and Ni) were identified where the considered phases had the lowest surface energy. The difference between the computed ground state energy and the surface free energy was bridged by approximating G in equation (1) by the DFT total energy E_{DFT}.[62] This substitution rests on the approximation that the contribution of the differences between the vibrational entropies of the surface and reference materials is small. Reutter and Scheffler have shown that these entropic differences for surface phases are typically similar in magnitude to the computational uncertainty of the ground state energies.[62] Replacing G with E_{DFT} gives the following equation for the surface free energy used in this work:

$$(2)\ \gamma(\{\mu_i\}) = \frac{1}{A}\left[E_{DFT} - \sum_i N_i\mu_i\right]$$

.

Chemical potentials

The chemical potentials μ_i (i = Si, O, and Ni) in equation (2) can be determined using the conditions under which the experiments were done. The oxygen chemical potential per atom was referenced to one half of the total energy of an isolated O_2 molecule at zero temperature. It is well known that DFT, and the PBE functional in particular, overestimates the O_2 binding energy.[63] Thus, instead of using one half of the O_2 DFT total energy, the oxygen chemical potential was referred to the DFT total energy of an oxygen atom plus one half of the experimental molecular O_2 atomization energy to provide a better comparison between theory and experiment. Experimental temperature and oxygen partial pressure were mapped to μ_O using standard thermochemical tables.[64] The determination of the Si chemical potential is more challenging: in principle, it can be approximated using the DFT total energy of crystalline Si at 0 K plus the integral of its heat capacity from 0 K to the temperature T of interest for bulk phase Si. This number would be of limited utility for comparison to the experiments where the supply of Si is in the form of a one-time fixed amount deposited rather than in the form of a constant vapor pressure under constant temperature (which leads to constant chemical potentials). Nonetheless, the relationship of Si chemical potential, μ_{Si}, increasing with increased Si availability still holds. The μ_{Si} in this paper is

referenced by the DFT total energy of bulk, diamond cubic Si per atom E_{DFT}^{Si}. Nickel atoms participating in the formation of the 2D surface phases of silicate are supplied by the alloy substrate. The alloy substrate is treated as an ideal binary solution in equilibrium with its constituent metals, making the chemical potential of nickel μ_{Ni} equal to the Gibbs free energy of bulk Ni per atom, which is later approximated by the DFT total energy of bulk Ni per atom, E_{DFT}^{Ni}.

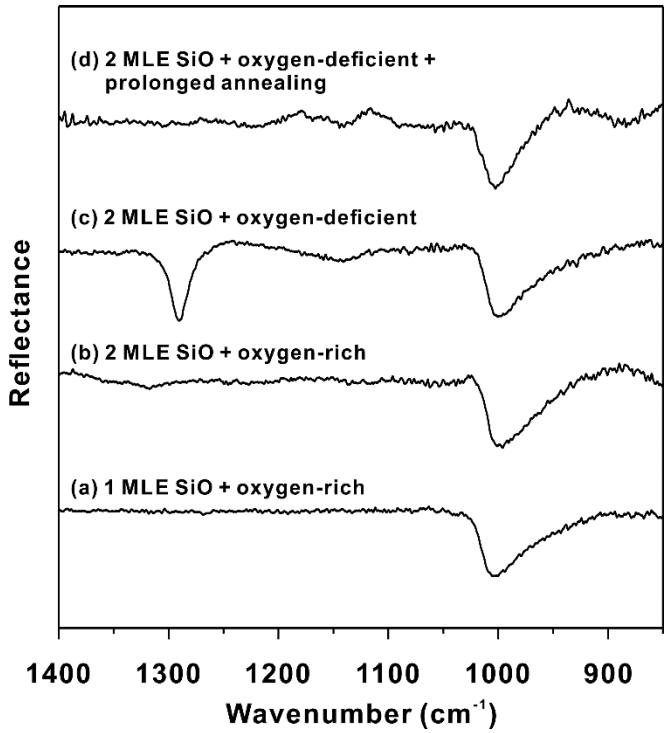

Figure 1. Reflection-absorption infrared spectra recorded following SiO deposition onto Ni_xPd_{1-x}(111) under different preparation conditions: (a) After depositing 1 MLE SiO on $Ni_{0.32}Pd_{0.68}$(111) in 2×10^{-6} Torr oxygen and annealing at 950 K in 2×10^{-6} Torr oxygen for 10

min; (b) after depositing 2 MLE SiO on $Ni_{0.32}Pd_{0.68}$(111) in 2×10^{-6} Torr oxygen and annealing at 950 K in 2×10^{-6} Torr oxygen for 10 min; (c) after depositing 2 MLE SiO on $Ni_{0.48}Pd_{0.52}$(111) in UHV and annealing at 950 K in 4×10^{-8} Torr oxygen for 5 min; (d) after further annealing the sample in (c) at 1000 K in 4×10^{-8} Torr oxygen for 10 min.

Results

1. Experimental Results

1.1 Impact of Growth Conditions

It was previously shown that a 2D Ni silicate forms on Ni_xPd_{1-x}(111) when 1 monolayer equivalent SiO is deposited in 2×10^{-6} Torr oxygen at 300 K and then annealed at 950 K in the same oxygen-rich environment.[50] Under such preparation conditions, 2D Ni silicate formation is a self-limited process and does not strongly depend on the substrate alloy composition. In the following context, substrates with compositions ranging from 52% to 93% Pd are referred to as Ni-Pd(111) without loss of generality. Here the objective was to determine if the Si-O-Ni bonding in the 2D Ni silicate could be avoided by varying the silica coverage, the oxygen partial pressure, and the annealing temperature, thereby producing 2D VDW silica. Reflection-absorption infrared spectroscopy is an effective technique to distinguish 2D Ni silicate from 2D VDW silica. Both experiment and theory have shown that the signature absorption peaks of Si–O stretches in Si–-

O–Ni linkage lie near 1000 cm^{-1},[50] while stretching the Si–O–Si bonds that connect the two halves of the bilayer features an absorption peak near 1300 cm^{-1} with small shifts depending on the substrate and the presence of adsorbates (O atoms) at the silica-metal interface.[29, 30, 37, 65] Theory indicates that the Si–O–Si interlayer vibration in 2D VDW silica will also appear near 1300 cm^{-1} on Ni-Pd(111).[50] Thus, RAIRS was employed to determine the structure of silica-containing overlayers prepared under various conditions.

Figure 1 compares the RAIRS spectra for a series of silica overlayers prepared under different conditions. Curve (a) in Figure 1 shows a typical RAIRS spectrum of 2D Ni silicate prepared by 1 MLE SiO deposition and annealing at 950 K in 2×10^{-6} Torr O_2 with a peak at 1000 cm^{-1}. For these growth conditions, no detectable change could be observed in the RAIRS spectrum within the alloy composition range studied (deposition onto pure Pd yields only the characteristic bilayer peak under these conditions[38]). As shown by Curve (b), increasing the amount of SiO deposited to 2 MLE while keeping the other growth conditions the same still produces the prominent 1000 cm^{-1} peak characteristic of 2D Ni silicate, with no evidence of the bilayer-associated peak near 1300 cm^{-1}. In this case, the excess silica forms clusters on top of Ni silicate monolayer which can be observed in STM. These bulk silica clusters may have a smaller IR cross-section or no preferred orientation for RAIRS, which would preclude their detection.

The high reactivity of Ni towards O compared to the metals on which 2D VDW silica has been observed (Cu,[66] Ru,[29] Pd[38, 39] and Pt[37]) suggests that Ni oxidation is the impediment to forming 2D VDW silica. Therefore, reducing the oxygen pressure to attempt to avoid Ni silicate formation was investigated. It was found that 4×10^{-8} Torr was the lowest O_2 pressure at which silica on Ni-Pd alloy substrates could be annealed above 900 K and remain on the surface without decomposition as determined by AES (See Supplement Fig. S1). Therefore, 2 MLE SiO was deposited onto Ni-Pd(111) substrates in UHV (background pressure less than 5×10^{-9} Torr) and then annealed in 4×10^{-8} Torr O_2 at 950 K for 5 minutes. Over the Pd composition range studied, no distinct differences could be observed in AES, RAIRS, and LEED measurements. Taking the film grown on $Ni_{0.48}Pd_{0.52}$ (111) substrate as a representative example, both the 2D VDW bilayer silica feature near 1300 cm^{-1} and the 2D Ni silicate feature near 1000 cm^{-1} could now be detected as shown in Figure 1 Curve (c), which indicates that reducing the oxygen pressure can inhibit Ni silicate formation. AES indicates that the Si is fully oxidized to Si^{4+} despite the low oxygen partial pressure (See Supplement Fig. S1).

The surface covered by co-existing 2D VDW silica and Ni silicate was further characterized by LEED and STM. As shown in Figures 2a, b, LEED patterns revealed both a diffraction ring and discrete spots with a spacing indicative of a long-range periodicity. Previous studies on metal-

supported 2D Ni, Ti and Fe silicates have shown similar long-range periodicity that originates from moiré features due to an incommensurate crystalline silicate phase.[47-50, 67] Meanwhile, similar ring features have been seen for amorphous 2D VDW silica on Pd(100),[35] Pt(111)[37], and Ru(0001).[31, 32] No amorphous transition metal silicate phases have been reported for either bulk or single layer materials.[68] Thus, the ring features in the LEED patterns can be tentatively attributed to amorphous 2D VDW silica.

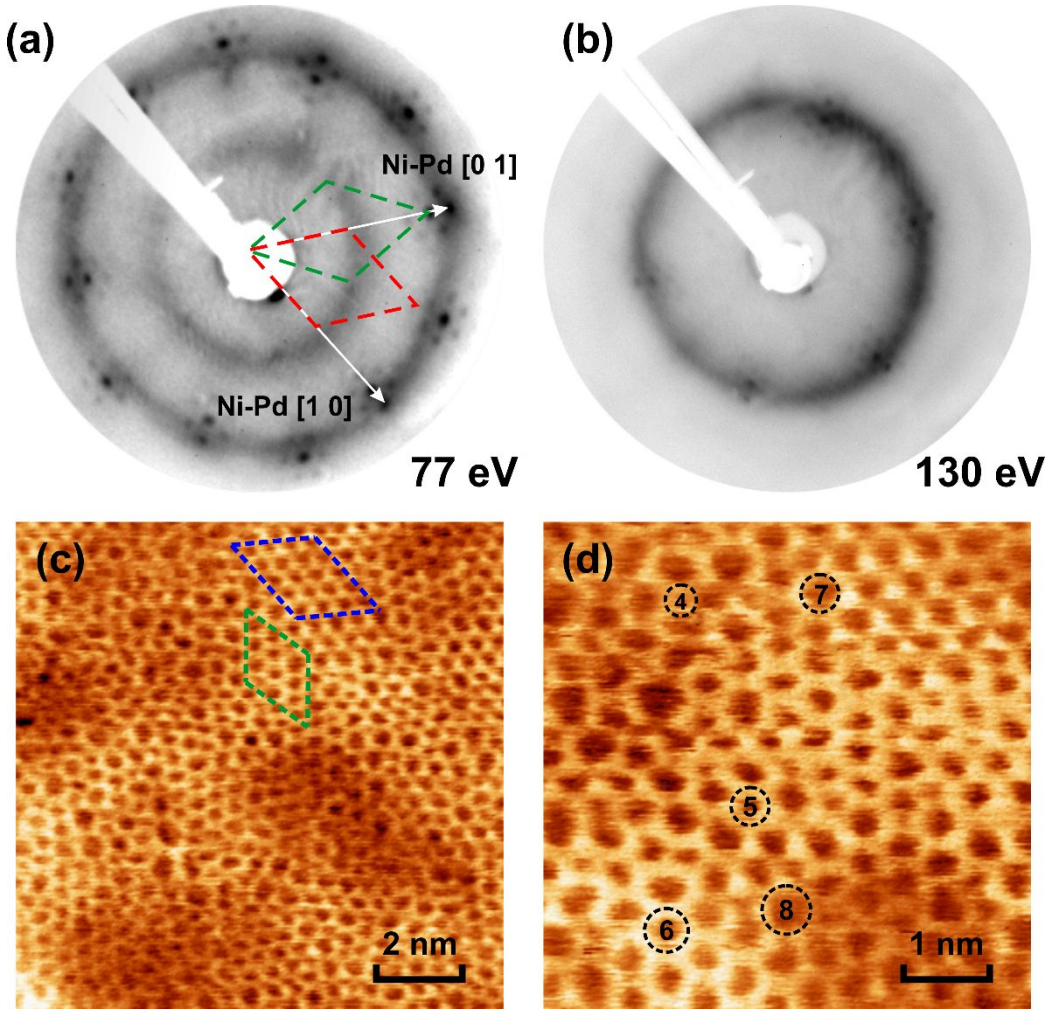

Figure 2. LEED and STM taken on the sample where Ni silicate and bilayer silica coexist. (a), (b): LEED patterns taken at different electron energies. The red and green dashed lines in (a) indicate the unit cells of commensurate and incommensurate Ni silicate phases in reciprocal space. The arrows show the primary directions of the substrate cells. (c), (d): STM images taken at different scales. Tip bias: 0.78 V. The green and blue dashed lines in (c) enclose two crystalline regions with different orientation. The circles and numbers in (d) indicate representative 4- to 8-member silica rings.

The corresponding STM images of the surface that gave the LEED patterns in Figures 2a, b demonstrate the coexistence of amorphous and crystalline regions. As shown in the wide range image in Figure 2c, the amorphous phase appears to cover most of the surface. Two small crystalline domains encompassing 12 and 16 unit cells are enclosed by green and blue dashed lines, respectively. The orientation of the two crystalline regions differ by nearly 30˚, matching the observation of two crystalline domains in LEED. Due to the limited extent of the crystalline regions, no moiré pattern could be seen with STM. As highlighted in the higher-resolution image in Figure 2d, the amorphous region is composed of four- through eight- membered rings which is typical of previous reports on 2D amorphous silica.[32, 69]

As noted above, the expectation is that the amorphous region corresponds to 2D VDW silica implying that Ni silicate is responsible for the crystalline regions. Silica, however, can exist in both amorphous and crystalline forms and it is difficult to distinguish crystalline silica from silicate as both show honeycomb patterns in STM images.[47-49] DFT calculations described in detail below indicate that the weaker VDW interaction of the 2D silica with the substrate is predicted to move the top honeycomb silica sheet 1.31 Å further from the metal surface; however, the chemical bonding of the Ni silicate to the substrate creates a stronger film-substrate electronic coupling which can offset the topographic height difference in STM images. In addition, the registry of the

overlayer with respect to the substrate also induces contrast variations.[50] The image in Figure 2c does not show uniform contrast with the crystalline domains tending to appear brighter or higher, but not uniformly so. Therefore, crystalline domains in the STM images cannot be unambiguously assigned to Ni silicate.

The effects of annealing time and temperature on the phases that form were also explored while holding the oxygen pressure at 4×10^{-8} Torr. Taking the mixed 2D silica/Ni silicate on $Ni_{0.48}Pd_{0.52}$ (111) system presented in Figure 2 as the starting point, the LEED patterns in Figure 3 reveal that another annealing with the temperature increased to 1000 K for 10 min caused the amorphous ring to disappear and the crystalline spots to become more prominent. This observation could be explained by the crystallization of amorphous 2D silica, the decomposition of 2D silica into volatile SiO and oxygen at high temperature and low oxygen pressure,[70] or the disproportionation of 2D silica into 2D Ni silicate plus 3D silica. The RAIRS data in Curve (d) Figure 1 recorded after the additional annealing reveals only the vibration associated with Ni silicate, eliminating 2D silica crystallization as a possibility. Increasing the oxygen pressure to 2×10^{-6} Torr while fixing the annealing temperature at 950 K also eliminated 2D silica vibrational features from a surface initially supporting co-existing 2D silica and Ni silicate. Since AES indicated no Si was lost from

the surface (See Supplement Fig. S1), this implies that 2D VDW silica can disproportionate into 2D Ni silicate plus 3D silica clusters.

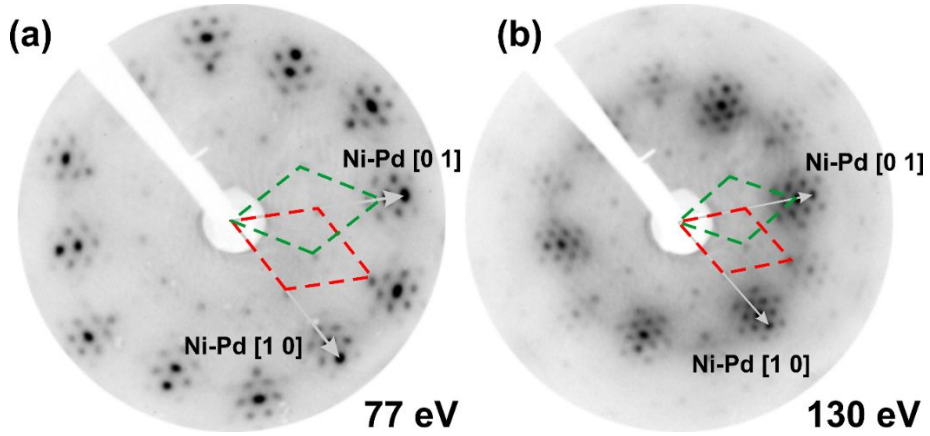

Figure 3. LEED patterns after annealing the sample shown in Figure 2 at 1000 K in 4×10^{-8} Torr oxygen for 10 min. The red and green dashed lines indicate the unit cells of the commensurate and incommensurate (i.e. 30° rotated) overlayer in reciprocal space. The arrows specify the substrate <10> directions.

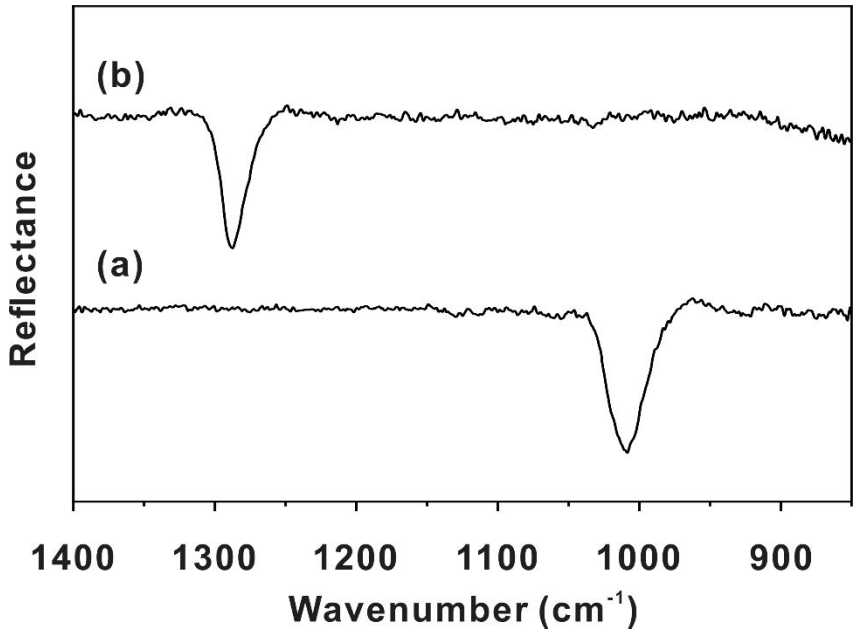

Figure 4. Comparison of RAIRS spectra for (a) SiO deposited onto $Ni_{0.07}Pd_{0.93}$(111) and annealed at 1000 K in 2×10^{-6} Torr O_2 and (b) 2D VDW silica on Pd(111). The peak position in (a) conveys 2D Ni silicate formation.

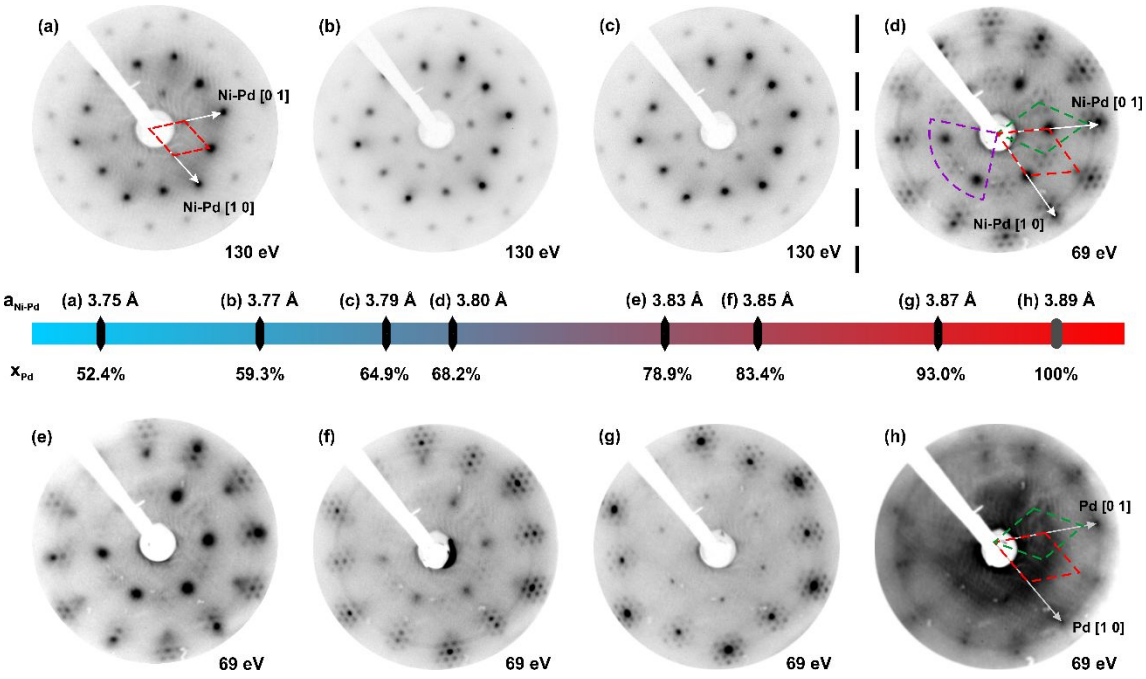

Figure 5. Commensurate-incommensurate transition of Ni silicate with respect to Ni-Pd(111) compositions shown by LEED results. (a)-(c) Ni silicate films with only commensurate crystalline phase. (d)-(g) Ni silicate films with the coexistence of incommensurate and commensurate crystalline phases. (h) 2D VDW silica with commensurate and incommensurate crystalline phases. In (a), (d) and (h), the red and green dashed lines indicate the unit cells of non-rotated and rotated overlayer phases in reciprocal space and the arrows show the primary directions of the substrates. The sector enclosed by the purple dashed line in (d) is better resolved by a LEEM system and is shown in Figure 6. The lattice constants of the Ni-Pd substrates and corresponding Pd compositions are labeled on the color bar.

1.2 Strain Effects on 2D Ni Silicate Formation

Previously, it was found that 1 MLE silica on Ni_xPd_{1-x}(111) can lead to a 2D Ni silicate over a range of Ni concentrations.[50] The prior work, however, also suggests that a commensurate phase forms on $Ni_{0.55}Pd_{0.45}$(111) with a surface lattice constant of 2.63 Å[40] and an incommensurate phase forms on $Ni_{0.26}Pd_{0.74}$(111) with a surface lattice constant 2.70 Å.[50] To find the maximum tensile mismatch strain that could be imparted, the structure of a series of overlayers was characterized as a function of alloy substrate composition. The annealing conditions, 1000 K in 2×10^{-6} Torr O_2 for 10 min, were selected to produce only the 2D Ni silicate as indicated by the representative RAIRS data in Figure 1. In addition, Figure 4 establishes that Ni silicate can form even when the alloy contains very little Ni: the RAIRS spectrum in Figure 4a for 7% Ni shows the characteristic Ni silicate feature near 1000 cm^{-1} while the spectrum in Figure 4b for elemental Pd(111) features the characteristic 2D VDW silica peak near 1300 cm^{-1}. Thus, any structural changes induced by increasing the Pd concentration in the alloy can be attributed to increased lattice mismatch.

Figure 5 shows a series of LEED patterns recorded as the substrate Pd concentration was varied between 52.4% and 100%, which covers tensile lattice mismatches between 0 and 3.8%. The patterns in Figures 5a-c, indicate a commensurate (2×2) structure and thus an epitaxially strained 2D Ni silicate layer. At larger mismatches, clusters of satellite spots appear in the LEED

patterns which reflect longer-range periodicities typical of an unstrained, incommensurate surface phase. Focusing on the pattern for $Ni_{0.32}Pd_{0.68}$(111) in Figure 5d, two sets of spots can be seen that are rotated 30° with respect to one another. In the figure, the green dashed lines highlight a reciprocal primitive unit cell of an overlayer rotated 30° with respect to the alloy substrate and the red dashed lines highlight an overlayer with its [10] direction aligned with that of the substrate. Satellite spots clearly surround the former, as would be expected since there is no small integer match between the expected 5.30 Å lattice constant of the silicate and $\sqrt{3}$ times the substrate surface lattice constant, 4.65 Å. Compared to the spots for R30° domain, the spots for the non-rotated domain appear more diffuse, suggesting that the spots corresponding to this domain may also be composed of closely spaced spots that could not be resolved. Better-resolved LEED patterns corresponding to the region enclosed by the purple dashed line in Figure 5d were recorded down to lower energies within a low energy electron microscopy (LEEM) system; the results are shown in Figure 6 for a beam energy of 15.7 eV. Here, satellite spots can be seen surrounding the (10) spots of both overlayer domains. The tighter spacing of the non-rotated domain is consistent with the small 1.40% mismatch, which leads to a longer-range moiré periodicity than the 30° rotated domain. The implication is that the 2D silicate has relaxed to its favored lattice constant in both domains. The coexistence of the rotated and non-rotated phases

can be observed in Figures 5d-f; however, the spots of the non-rotated phase became dimmer as the substrate lattice constant increased, and in Figure 5g, it is difficult to distinguish the non-rotated phase. Thus, the results indicate an increasing preference for the rotated phase as the mismatch increases. For completeness, LEED data for 2D VDW silica on pure Pd(111) are shown in Figure 5h. In this case the LEED pattern is much more diffuse with comparatively blurry satellite spots, but the data still point to a crystalline incommensurate phase, which matches previously reported results.[38] For the following reasons changes in alloy chemistry as the Ni content was varied can be ruled out as responsible for the observed commensurate to incommensurate transition: the transition occurs over a change in Ni substrate concentration of just 3.3%; AES indicates a Ni rich interface under the experimental conditions thereby mitigating the impact of small changes in the bulk composition on the surface chemistry; RAIRS indicates that 2D Ni silicate forms under the growth conditions if the substrate contains any Ni at all; and prior theoretical work indicates the same general Ni silicate structure when the substrate alloy composition is changed.[50] Taken together, the data reveal a transition from strained commensurate to relaxed incommensurate 2D Ni silicate between substrate lattice constants of 3.79 Å (2.68 Å surface lattice constant) and 3.80 Å (2.69 Å surface lattice constant). Presuming a typical single sheet layered silicate lattice constant of 5.30 Å, this corresponds to a tensile lattice strain between 1.12% and 1.40%.

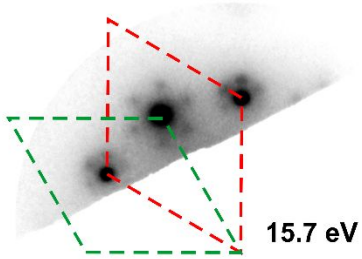

Figure 6. High-resolution LEED patterns corresponding to the region enclosed by the purple dashed line in Figure 5d. The red and green dashed lines indicate the unit cells of two crystalline regions: (i) the non-rotated phase (red) and (ii) the phase rotated by 30° (green).

Scanning tunneling microscopy data reinforce the conclusions drawn from the LEED data. Representative STM images recorded above and below the phase transition are provided in Figure 7, with panel (a) featuring a honeycomb structure with no long-range structure, consistent with a commensurate (2×2) structure, while panel (b) reveals a moiré pattern superimposed on a hexagonal atomic-scale structure. Finally, the image in panel (c) exposes the six-membered ring structure of crystalline 2D VDW silica on Pd(111); here, the contrast variations are induced by lattice mismatch, which is similar to the contrast variations observed in Ni silicate.[50]

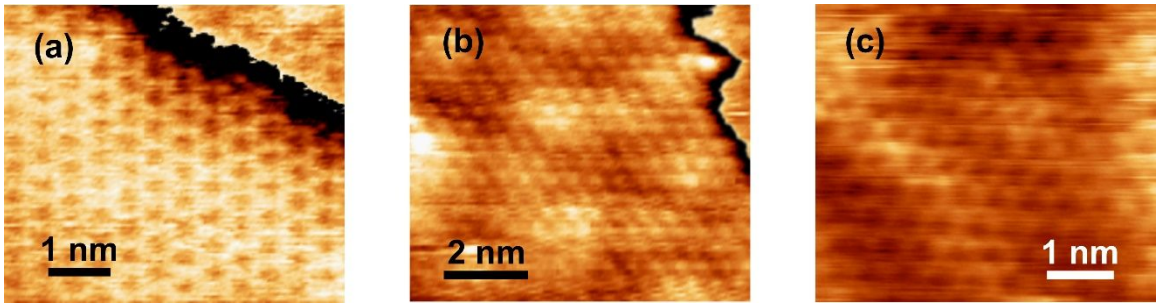

Figure 7. Scanning tunneling microscopy images taken on (a) commensurate crystalline Ni silicate on $Ni_{0.48}Pd_{0.52}$(111); (b) incommensurate crystalline Ni silicate on $Ni_{0.26}Pd_{0.74}$(111); and (c) incommensurate crystalline 2D VDW silica on Pd(111). Tip bias: (a) 2.35 V, (b) 0.80 V, (c) -0.30 V.

It should be noted that the 2D Ni silicate formed directly on $Ni_{0.48}Pd_{0.52}$ (111) in oxygen rich environments yields only commensurate (2×2) domains (Figure 5a) while the LEED patterns in Figures 2 and 3 reveal the presence of the rotated incommensurate phase when the surface passes through a state in which 2D VDW silica and 2D Ni silicate coexist. The potential reasons for these differences will be addressed in the Discussion section.

2. Computational Results

2.1 Competition Between 2D Silica and Silicate Phases on Ni-Pd(111)

The thrust of the theoretical effort was to understand how the growth conditions influence whether 2D silica or Ni silicate forms on the alloy surface and thus only 2D surface phases were

considered. Because these transitions are observed even when the lattice mismatch is minimal, the focus was on commensurate (2×2) phases. Prior work indicates only small energy differences between amorphous and crystalline 2D VDW silica,[22] justifying consideration of crystalline SiO_2 rather than the observed amorphous phase. Although the experimental evidence suggests that 2D VDW silica can disproportionate into 2D Ni silicate plus 3D silica, modeling this situation would require detailed knowledge of the exposed 3D silica cluster facets and their surface and interfacial energies, which are beyond the scope of this paper. The alloy composition chosen was $Ni_{0.5}Pd_{0.5}$ because twice its computed (111) surface lattice (5.29 Å) is a good match to twice that of theoretical free-standing 2D silica (5.27 Å) and 2D layered Ni silicate in the trioctahedral clay form (5.30 Å). The computed alloy lattice constant matches the experimental value within a few thousandths of an Ångstrom.[40, 50] As shown in Figure 5, in this alloy composition range the 2D Ni silicate forms a commensurate (2×2) structure. Consistent with this observation, the 2D phases were modeled using either the rectangular $(2 \times 2\sqrt{3})$ surface unit cell or the hexagonal (2×2) surface unit. Enforcing the epitaxial match imposes a negligible strain on the 2D layers, i.e. only 0.3% tensile strain on the 2D VDW silica. Structures selected for the 2D phase diagram calculation included: the bare alloy surface, a Si_2O_5 monolayer, bilayer VDW SiO_2, and Ni silicate, all with and without an additional chemisorbed oxygen atom per (2×2) surface unit cell (Figure 8). All

silica or silicate overlayers are assumed to sit on a Ni monolayer atop the alloy substrate because AES data show Ni segregation to the interface following SiO deposition and high temperature annealing.[50] Layers with Si–O–Pd bonds were not considered because: no evidence of such linkages have been seen when silica is deposited onto pure Pd;[38, 39] Pd clays are not known to exist; and the AES data indicates Ni segregation to the interface.[50] Structural models for monolayer and bilayer silica (Figures 8c-f) were taken from previous work.[29, 30] The atomic structure of Ni silicate thin film has been the subject of our prior work.[50] In the fully relaxed Ni silicate thin film (Figures 8g, h), a sheet of Si tetrahedra is stacked over a nickel oxide sheet that couples to the alloy substrate through the Ni–O–Substrate chemical bonds. The Si and Ni atoms both form hexagonal six-membered rings within their own sheet, but the two sets of the six-membered rings have a rigid shift in the x-y plane, unlike the bilayer silica where the six-membered rings in the top and bottom sheets are aligned (Figures 8e, f).

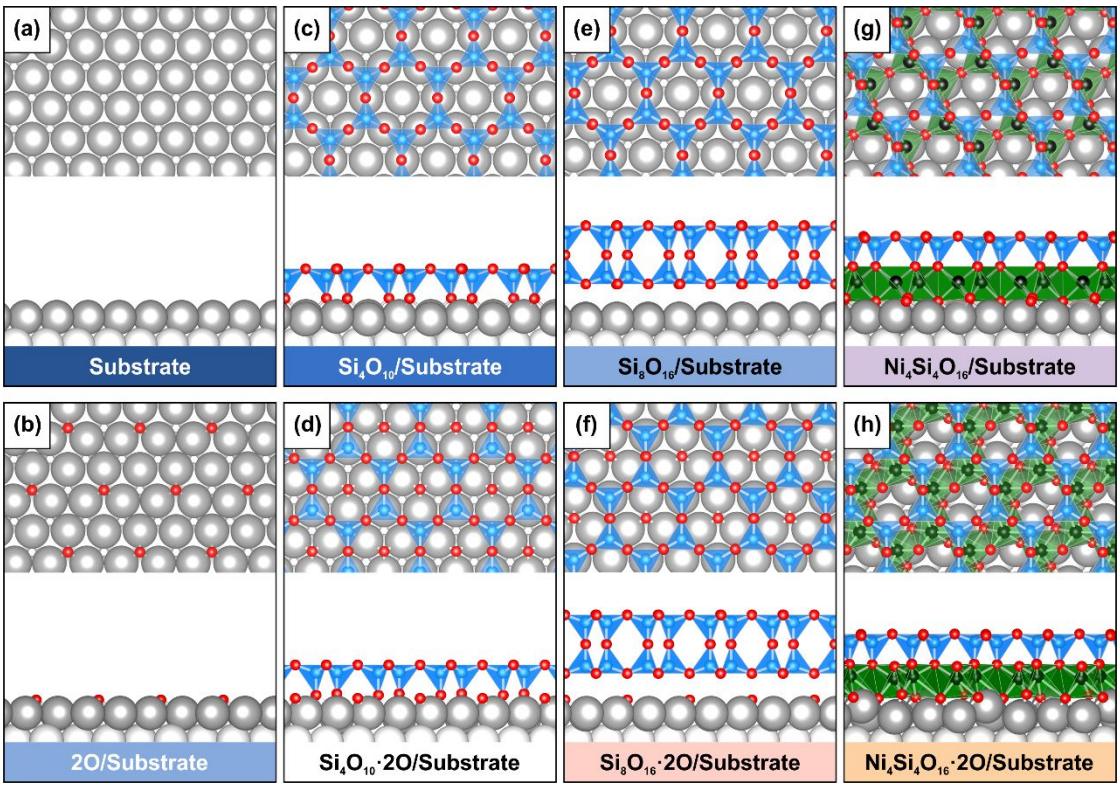

Figure 8 Atomic structures of 2D surface phases on the $Ni_{0.5}Pd_{0.5}$ alloy substrate (chemical formulae are defined per $(2 \times \sqrt{3})$ surface unit cell): (a) Substrate (clean surface), (b) 2O/Substrate (one chemisorbed oxygen on the hollow site), (c) Si_4O_{10}/Substrate (monolayer silica), (d) Si_4O_{10}•2O/Substrate (monolayer silica with one chemisorbed oxygen), (e) Si_8O_{16}/Substrate (bilayer silica), (f) Si_8O_{16}•2O/Substrate (bilayer silica with one chemisorbed oxygen), (g) $Ni_4Si_4O_{16}$/Substrate (Ni silicate), and (h) $Ni_4Si_4O_{16}$•2O/Substrate (Ni silicate with one chemisorbed oxygen). Oxygen polyhedra are drawn to emphasize the neighboring oxygen atoms surrounding the Si and Ni atoms in the 2D thin film. Color scheme: Si cyan, O red, Ni (in the

overlayer) black, Ni (on the substrate surface) grey, $Ni_{0.5}Pd_{0.5}$ VCA atom white. Background color under each chemical formula corresponds to the color of region in the phase diagram in Figure 9.

2.2 Phase Diagram

Predictions of the stable 2D phases on the $Ni_{0.5}Pd_{0.5}$ alloy are compiled in the 2D surface phase diagram displayed in Figure 9. The axes of the chemical potentials of Si and O were centered around the references detailed in the Computational Methods section using the following transformation:

$$\Delta\mu_{Si} = \mu_{\mathrm{Si}} - E^{\mathrm{Si}}_{\mathrm{DFT}} \quad (3)$$

$$\Delta\mu_{\mathrm{O}} = \mu_{\mathrm{O}} - E^{\mathrm{O\ atom}}_{\mathrm{DFT}} - E^{\mathrm{O_2\ atomization}}_{\mathrm{Exp}}/2 \quad (4)$$

The different colors in the phase diagram correspond to the most stable phase at any given pair of $\Delta\mu_{\mathrm{Si}}$, $\Delta\mu_{\mathrm{O}}$. Throughout, μ_{Ni} was fixed at the DFT total energy of bulk Ni per atom as explained below. The experiments were done under UHV and high annealing temperature (~1000 K), which makes the range of the oxygen chemical potential of interest negative. The values of $\Delta\mu_{\mathrm{O}}$ relevant to the typical experimental conditions (e.g., annealing temperature between 900 K and 1100 K and oxygen partial pressure between 4×10^{-8} Torr and 2×10^{-6} Torr) in this work range from –1.80 eV to –2.20 eV. Since zero valent Si was never experimentally observed, the regime of interest is $\Delta\mu_{\mathrm{Si}} < 0$. In fact, the Si AES peak remained consistent with SiO_2 in the lower oxygen pressure

annealing experiments (See Supplement Fig. S1). Experimental conditions where 2D free-standing VDW bilayer silica can be stabilized over its decomposition into Si and O atoms that returns to the reservoirs were also used; this means μ_O and μ_{Si} should obey the inequality:

$$\mu_{Si} + 2\mu_O > E_{DFT}^{\text{free-standing bilayer } SiO_2} \quad (5)$$

The region above the dashed line in Figure 9 corresponds to the combination of μ_O and μ_{Si} that satisfies equation (5). All the constraints on μ_O and μ_{Si} discussed above define the experimentally accessible region in the phase diagram, shown as the area encompassed by the solid line in Figure 9. The main conclusion drawn from the phase diagram is that the thermodynamically stable phases on $Ni_{0.5}Pd_{0.5}$ in this study are either bilayer silica with surface chemisorbed oxygen or Ni silicate; their relative stability depends on the Si supply, i.e., a larger amount of Si favors the 2D VDW silica phase. However, the system might be kinetically trapped in other phases. The phase diagram also points to another route for achieving 2D VDW silica on the surface. Instead of just increasing the silicon supply, one can decrease $\Delta\mu_O$ to –3.50 eV (e.g. by increasing the annealing temperature of the system to 1500 K while keeping the oxygen partial pressure at 4×10^{-8} Torr) to ensure that the Ni silicate is no longer stable during the growth procedure.

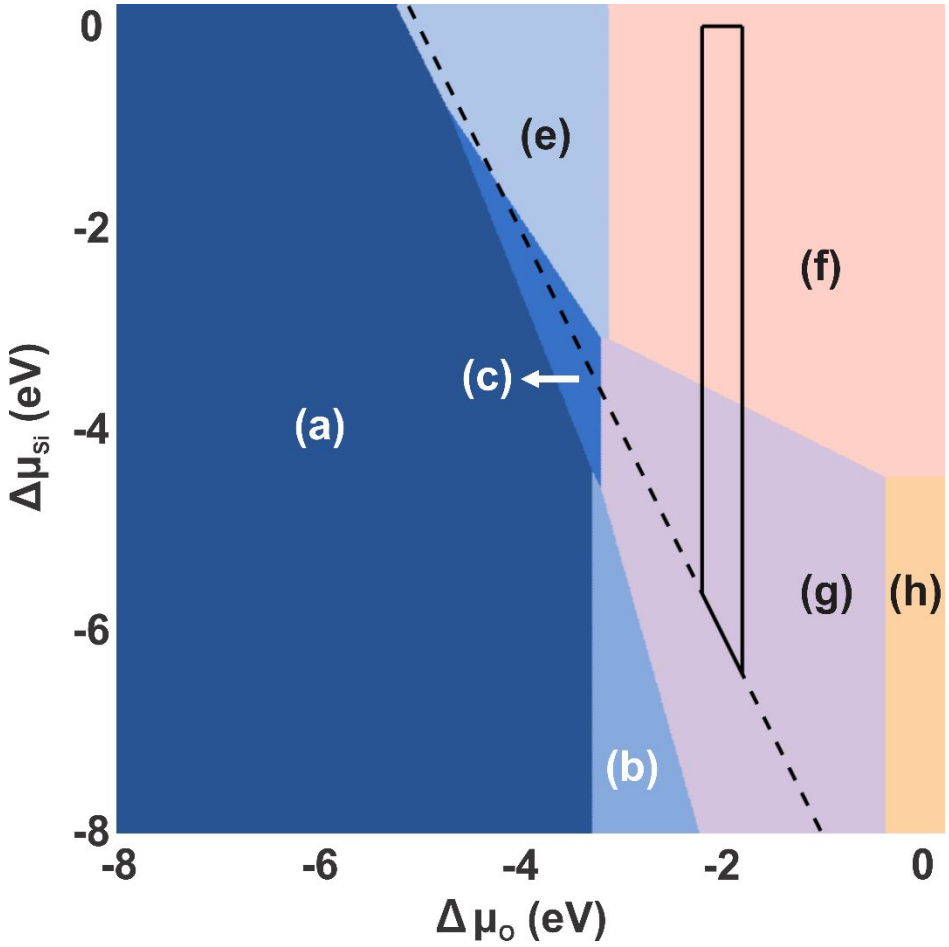

Figure 9 Phase diagram for the silica/silicate 2D surface phases on the $Ni_{0.5}Pd_{0.5}$ alloy substrate. Each colored region corresponds to the thermodynamically stable surface phase based on the surface free energy as a function of the Si and O chemical potentials. Letters denoting different phases follow the same notation as Figure 8. The bilayer silica can be stabilized above the black dashed line on the surface. The experimentally accessible region of the chemical potentials in this study is inside of the black solid lines.

Discussion

Growth on the single crystal, solid solution alloy substrate enabled the systematic experimental determination of how much strain can be imparted to an atomically thin 2D layer without appreciably changing the chemistry of the interfacial interactions. Despite the existence of chemical bonds between the 2D Ni silicate and the alloy substrate, the results reveal that 2D Ni silicate overlayers can only be tensilely strained between 1.12% and 1.40% before the material relaxes to its favored lattice constant. This strain is less than the 2.1% tensile strain that Ru(0001) can impart to 2D silica bilayers despite much weaker VDW film-substrate interactions for SiO_2/Ru(0001). Therefore, the overall strength of the film–substrate interaction must not have been the decisive factor in determining how much epitaxial strain could be applied to the 2D layer. Rather, the results highlight the importance of: 1) the 2D modulus (stiffness) of the 2D overlayer; 2) the accessibility of other phases that can relieve the strain; and 3) the energy penalty for incommensuration. For 2D Ni silicate all three appear to limit the strain that can be applied. Regarding the 2D modulus, tetrahedral 2D bilayers can be relatively easily distorted by increasing tetrahedral bond angles, a low-energy distortion which is limited by connections to the octahedrally coordinated Ni–O layer in 2D Ni silicate.[22, 39, 71] While SiO_2 can easily access a range

of structures with varying ring sizes,[22] the clay family to which 2D Ni silicate belongs is solely based on a sheet of six-membered rings of corner-sharing SiO_4 tetrahedra. Finally, concerning the energy penalty for incommensuration, our prior theoretical study of the 2D Ni silicate structure revealed only a maximum 80 meV energy penalty to shift the silicate away from its favored registry with the substrate.[50] This finding indicates that it is the variation in the strength of the 2D material–substrate interaction as the 2D material is shifted with respect to the substrate that is important to determining the amount of epitaxial strain that can be applied to a 2D material, not the overall magnitude of the 2D material–substrate interaction.

A curious aspect of the results was the experimental finding that reducing the oxygen pressure during annealing facilitated the formation of 2D VDW silica, but that even at lower oxygen pressures the 2D VDW silica eventually completely converted to 2D Ni silicate. This is at odds with the expectations from the theoretical phase diagram which suggests that under the experimental conditions only 2D VDW silica should form when there is sufficient Si, which the initial observation of 2D VDW silica suggests there clearly was. This apparent discrepancy may be due to limitations of the thermodynamic model. In particular, the model did not include bulk SiO_2 and so it may be that bulk SiO_2 plus Ni silicate is favored at high silicon coverages and the high experimental temperatures. In addition, the model assumes a uniform surface that can freely

exchange species with reservoirs of atoms. While this may accurately reflect the situation for oxygen, for silicon it is clearly not the case. Rather, the actual surface contains a fixed amount of Si, since the experimental conditions were limited to those where Si was not lost from the surface, with some degree of mobility at the high annealing temperatures. At the high temperatures, density fluctuations may lead to regions of locally low Si concentrations where the 2D Ni silicate is favored and other regions with locally higher Si concentrations where bulk 3D silica forms.[39, 47] If either of these transformations is kinetically irreversible, then the 2D Ni silicate decorated by 3D silica clusters will eventually cover the entire surface.

The experimental and theoretical results point to directions to create either 2D Ni silicate or 2D VDW silica on demand. The former can be readily realized by depositing 1 MLE SiO and annealing above 950 K while the latter presents more of a challenge. One approach to obtaining solely 2D VDW silica is to simply reduce the annealing time from minutes to seconds; unfortunately, the thermal mass of the sample assembly and limitations of the heater dictated relatively slow heating and cooling so that the sample spent at least minutes near the ultimate annealing temperature. As pointed out in the preceding section, a more robust way to produce only 2D VDW silica would be to reduce the oxygen chemical potential to the region where the Ni silicate is not favored regardless of the Si chemical potential. Although the dashed line in the

phase diagram in Figure 9 suggests that these oxygen chemical potentials overlap regions where silica will not decompose, experiments suggest that this will be challenging as it was found that the lowest oxygen pressure at which Si remained at the surface at the relevant temperatures was 4×10^{-8} Torr. Nonetheless, experiments at higher temperatures in a SiO flux that can replenish Si lost from the surface can potentially access this region of the phase diagram where Ni silicate formation can be avoided.

There are also curious aspects of the structures that form at lower oxygen partial pressures. First, amorphous 2D VDW silica formed despite near zero lattice mismatch, apparently at odds with reports for Pt(111) and Pd(111) which suggested that large mismatch favors amorphous structures.[37, 72] Previous research, however, also highlights the roles of sample cooling rate after high-temperature annealing, the initial amount of silicon, the annealing temperature, and the oxygen partial pressure in determining crystallinity.[31, 32, 35, 73] The results presented here indicate that these factors are at least as important as the lattice match in determining the competition between the crystalline and amorphous phases. Perhaps more interestingly, it was found that the 2D Ni silicate that formed at lower oxygen pressures (where its formation proceeds at least in part through 2D VDW silica) aligns differently with the substrate than 2D Ni silicate formed directly at higher oxygen partial pressures: the former is rotated 30°

and is incommensurate while the latter is commensurate. This difference is likely due to a combination of a small driving force for commensuration and a different Ni silicate nucleation process at the different oxygen pressures. Regarding the former, the prior theoretical study on the 2D Ni silicate structure revealed that the energy cost of incommensuration is modest.[50] Meanwhile, the initial silica deposition near room temperature produces a three-dimensionally disordered structure that is presumably defect rich. The annealing temperature is insufficient to melt bulk silica but apparently allows enough mobility to access lower energy states.[74] At higher oxygen pressures, the results suggest that the 2D Ni silicate nucleates from the 3D disordered state which appears to allow sufficient reversibility of small cluster formation to access the lower energy commensurate state (for small lattice mismatch). On the other hand, the 2D VDW bilayer silica structure removes defects, reducing the system energy and presumably increasing the barrier to motion and bond rearrangement. As a result, nucleation of the Ni silicate from 2D VDW silica may be limited to weak points in the structure such as at large rings or crystalline domain boundaries with the consequence that the Ni silicate forms where it can with a high probability of incommensuration as opposed to sampling many sites in a more defective three-dimensionally disordered network. Finally, the incommensurate Ni silicate did not disappear after longer annealing times at a higher temperature, indicating that once it forms, it cannot convert back to

2D VDW silica or transit into the commensurate phase under the experimentally accessible conditions.

Summary

Combining STM, LEED, RAIRS, DFT, and *ab initio* thermodynamics, the competition between the formation of multiple 2D VDW silica and 2D Ni silicate phases on Ni-Pd solid solution alloy substrates was systematically investigated. While only 2D Ni silicate was observed under oxygen-rich conditions during high-temperature annealing, limiting the oxygen pressure during each film growth step suppressed silicate formation and allowed 2D VDW silica to form. DFT was employed to explain the experimental findings from a thermodynamic perspective. The *ab initio* phase diagram highlighted the preference for 2D VDW silica under silicon-rich, oxygen-lean conditions. Despite the theoretical implication that a surface exposing only 2D VDW silica phase can be thermodynamically favored, experiments showed that the 2D VDW silica phase eventually disproportionated into 3D silica and 2D Ni silicate at high temperatures. Theory suggests that the disproportionation reaction may be avoided by decreasing the oxygen chemical potential during annealing (through a combination of increasing the temperature and decreasing the oxygen pressure) while replenishing any silica lost from the surface. Varying the solid solution alloy

substrate composition allowed the effect of strain on the structure of the 2D Ni silicate to be studied without significantly changing the interfacial chemistry. A commensurate to incommensurate transition was observed between 1.12% and 1.40% tensile mismatch, pinpointing the maximum epitaxial tensile strain within ±0.14%. The relaxation at relatively small strains despite the presence overlayer–substrate chemical bonds highlights the importance of the stiffness of the 2D layer and the driving force for commensuration in determining the maximum epitaxial strain rather than just the strength of the overlayer–substrate interaction. This research demonstrates several pathways to engineer the phase and structure of 2D silica and silicates that can be potentially employed to other 2D materials systems.

Acknowledgments

Computing resources were provided by the Yale University Faculty of Arts and Sciences High-Performance Computing Center and by the National Science Foundation XSEDE program via grant TG-MCA08X007. Initial RAIRS measurements were carried out at the Center for Functional Nanomaterials which is a U.S. DOE Office of Science Facility at Brookhaven National Laboratory under Contract No. DE-SC0012704. J.-H. Jhang acknowledges the support of the U.S. Department of Energy through Basic Energy Sciences grant DE-SC0014414 for his effort on this paper. This project was supported by National Science Foundation Grant DMR 1506800.

References

1. A. K. Geim and I. V. Grigorieva, *Nature*, 2013, **499**, 419-425.
2. X. Wang and F. Xia, *Nat Mater*, 2015, **14**, 264-265.
3. K. S. Novoselov, A. Mishchenko, A. Carvalho and A. H. Castro Neto, *Science*, 2016, **353**, aac9439.
4. S. Jin, M. Huang, Y. Kwon, L. Zhang, B. W. Li, S. Oh, J. Dong, D. Luo, M. Biswal, B. V. Cunning, P. V. Bakharev, I. Moon, W. J. Yoo, D. C. Camacho-Mojica, Y. J. Kim, S. H. Lee, B. Wang, W. K. Seong, M. Saxena, F. Ding, H. J. Shin and R. S. Ruoff, *Science*, 2018, **362**, 1021-1025.
5. I. V. Vlassiouk, Y. Stehle, P. R. Pudasaini, R. R. Unocic, P. D. Rack, A. P. Baddorf, I. N. Ivanov, N. V. Lavrik, F. List, N. Gupta, K. V. Bets, B. I. Yakobson and S. N. Smirnov, *Nat Mater*, 2018, **17**, 318-322.
6. S. Z. Butler, S. M. Hollen, L. Cao, Y. Cui, J. A. Gupta, H. R. Gutierrez, T. F. Heinz, S. S. Hong, J. Huang, A. F. Ismach, E. Johnston-Halperin, M. Kuno, V. V. Plashnitsa, R. D. Robinson, R. S. Ruoff, S. Salahuddin, J. Shan, L. Shi, M. G. Spencer, M. Terrones, W. Windl and J. E. Goldberger, *ACS Nano*, 2013, **7**, 2898-2926.
7. M. Xu, T. Liang, M. Shi and H. Chen, *Chem Rev*, 2013, **113**, 3766-3798.
8. G. R. Bhimanapati, Z. Lin, V. Meunier, Y. Jung, J. Cha, S. Das, D. Xiao, Y. Son, M. S. Strano, V. R. Cooper, L. Liang, S. G. Louie, E. Ringe, W. Zhou, S. S. Kim, R. R. Naik, B. G. Sumpter, H. Terrones, F. Xia, Y. Wang, J. Zhu, D. Akinwande, N. Alem, J. A. Schuller, R. E. Schaak, M. Terrones and J. A. Robinson, *ACS Nano*, 2015, **9**, 11509-11539.
9. A. Ambrosi, Z. Sofer and M. Pumera, *Chem Commun (Camb)*, 2015, **51**, 8450-8453.
10. H. H. Huang, X. Fan, D. J. Singh, H. Chen, Q. Jiang and W. T. Zheng, *Phys Chem Chem Phys*, 2016, **18**, 4086-4094.

11. A. J. Mannix, B. Kiraly, M. C. Hersam and N. P. Guisinger, *Nature Reviews Chemistry*, 2017, **1**, 0014.

12. J. A. del Alamo, *Nature*, 2011, **479**, 317-323.

13. S. Yang, F. Liu, C. Wu and S. Yang, *Small*, 2016, **12**, 4028-4047.

14. M. Luo and S. Guo, *Nature Reviews Materials*, 2017, **2**.

15. Z. Dai, L. Liu and Z. Zhang, *Adv Mater*, 2019, DOI: 10.1002/adma.201805417, e1805417.

16. P. Y. Huang, C. S. Ruiz-Vargas, A. M. van der Zande, W. S. Whitney, M. P. Levendorf, J. W. Kevek, S. Garg, J. S. Alden, C. J. Hustedt, Y. Zhu, J. Park, P. L. McEuen and D. A. Muller, *Nature*, 2011, **469**, 389-392.

17. P. W. Sutter, J. I. Flege and E. A. Sutter, *Nat Mater*, 2008, **7**, 406-411.

18. J. Wintterlin and M. L. Bocquet, *Surface Science*, 2009, **603**, 1841-1852.

19. H. Terrones, M. Terrones, E. Hernandez, N. Grobert, J. C. Charlier and P. M. Ajayan, *Phys Rev Lett*, 2000, **84**, 1716-1719.

20. Z. G. Fthenakis and N. N. Lathiotakis, *Phys Chem Chem Phys*, 2015, **17**, 16418-16427.

21. Y. Wang, A. J. Page, Y. Nishimoto, H. J. Qian, K. Morokuma and S. Irle, *J Am Chem Soc*, 2011, **133**, 18837-18842.

22. A. Malashevich, S. Ismail-Beigi and E. I. Altman, *The Journal of Physical Chemistry C*, 2016, **120**, 26770-26781.

23. E. Gao, B. Xie and Z. Xu, *Journal of Applied Physics*, 2016, **119**.

24. S. Shaikhutdinov and H. J. Freund, *Adv Mater*, 2013, **25**, 49-67.

25. S. Shaikhutdinov and H. J. Freund, *Journal of physics. Condensed matter : an Institute of Physics journal*, 2015, **27**, 443001.

26. C. Buchner and M. Heyde, *Prog Surf Sci*, 2017, **92**, 341-374.

27. B. Yang, J. A. Boscoboinik, X. Yu, S. Shaikhutdinov and H. J. Freund, *Nano letters*, 2013, **13**, 4422-4427.

28. T. Bjorkman, S. Kurasch, O. Lehtinen, J. Kotakoski, O. V. Yazyev, A. Srivastava, V. Skakalova, J. H. Smet, U. Kaiser and A. V. Krasheninnikov, *Sci. Rep.*, 2013, **3**, 3482.

29. D. Loffler, J. J. Uhlrich, M. Baron, B. Yang, X. Yu, L. Lichtenstein, L. Heinke, C. Buchner, M. Heyde, S. Shaikhutdinov, H. J. Freund, R. Wlodarczyk, M. Sierka and J. Sauer, *Phys Rev Lett*, 2010, **105**, 146104.

30. B. Yang, W. E. Kaden, X. Yu, J. A. Boscoboinik, Y. Martynova, L. Lichtenstein, M. Heyde, M. Sterrer, R. Wlodarczyk, M. Sierka, J. Sauer, S. Shaikhutdinov and H. J. Freund, *Phys Chem Chem Phys*, 2012, **14**, 11344-11351.

31. L. Lichtenstein, M. Heyde and H. J. Freund, *J Phys Chem C*, 2012, **116**, 20426-20432.

32. L. Lichtenstein, M. Heyde and H. J. Freund, *Phys Rev Lett*, 2012, **109**, 106101.

33. M. Heyde, S. Shaikhutdinov and H. J. Freund, *Chemical Physics Letters*, 2012, **550**, 1-7.

34. L. Lichtenstein, C. Buchner, B. Yang, S. Shaikhutdinov, M. Heyde, M. Sierka, R. Wlodarczyk, J. Sauer and H. J. Freund, *Angew Chem Int Ed Engl*, 2012, **51**, 404-407.

35. E. I. Altman and U. D. Schwarz, *Adv Mater Interfaces*, 2014, **1**, 1400108.

36. K. M. Burson, C. Buchner, M. Heyde and H. J. Freund, *Journal of physics. Condensed matter : an Institute of Physics journal*, 2017, **29**, 035002.

37. Y. Xin, B. Yang, J. A. Boscoboinik, S. Shaikhutdinov and H. J. Freund, *Appl. Phys. Lett.*, 2012, **100**, 151608.

38. J. H. Jhang, C. Zhou, O. E. Dagdeviren, G. S. Hutchings, U. D. Schwarz and E. I. Altman, *Phys Chem Chem Phys*, 2017, **19**, 14001-14011.

39. E. I. Altman, J. Gotzen, N. Samudrala and U. D. Schwarz, *J Phys Chem C*, 2013, **117**, 26144-26155.

40. G. S. Hutchings, J. H. Jhang, C. Zhou, D. Hynek, U. D. Schwarz and E. I. Altman, *ACS Appl Mater Interfaces*, 2017, **9**, 11266-11271.

41. G. Ghosh, C. Kantner and G. Olson, *Journal of phase equilibria*, 1999, **20**, 295.

42. J. Weissenrieder, S. Kaya, J. L. Lu, H. J. Gao, S. Shaikhutdinov, H. J. Freund, M. Sierka, T. K. Todorova and J. Sauer, *Phys Rev Lett*, 2005, **95**, 076103.

43. M. Chen and D. W. Goodman, *Surface Science*, 2006, **600**, L255-L259.

44. T. K. Todorova, M. Sierka, J. Sauer, S. Kaya, J. Weissenrieder, J. L. Lu, H. J. Gao, S. Shaikhutdinov and H. J. Freund, *Physical Review B*, 2006, **73**.

45. J. W. Anthony, R. A. Bideaux, K. W. Bladh and M. C. Nichols, *Handbook of Mineralogy*, 2000.

46. S. M. Auerbach, K. A. Carrado and P. K. Dutta, *Handbook of Zeolite Science and Technology*, CRC press, 2003.

47. R. Wlodarczyk, J. Sauer, X. Yu, J. A. Boscoboinik, B. Yang, S. Shaikhutdinov and H. J. Freund, *J Am Chem Soc*, 2013, **135**, 19222-19228.

48. F. D. Fischer, J. Sauer, X. Yu, J. A. Boscoboinik, S. Shaikhutdinov and H. J. Freund, *J Phys Chem C*, 2015, **119**, 15443-15448.

49. H. Tissot, L. Li, S. Shaikhutdinov and H. J. Freund, *Phys Chem Chem Phys*, 2016, **18**, 25027-25035.

50. C. Zhou, X. Liang, G. S. Hutchings, Z. S. Fishman, J.-H. Jhang, M. Li, U. D. Schwarz, S. Ismail-Beigi and E. I. Altman, *Chemistry of Materials*, 2019, **31**, 851-861.

51. A. Nash and P. Nash, *Bulletin of Alloy Phase Diagrams*, 1984, **5**, 446-450.

52. C. Y. Nakakura, V. M. Phanse, G. Zheng, G. Bannon, E. I. Altman and K. P. Lee, *Rev. Sci. Instrum.*, 1998, **69**, 3251.

53. P. Hohenberg and W. Kohn, *Phys. Rev.*, 1964, **136**, B864-B871.

54. W. Kohn and L. J. Sham, *Phys. Rev.*, 1965, **140**, A1133-A1138.

55. J. P. Perdew, K. Burke and M. Ernzerhof, *Physical Review Letters*, 1996, **77**, 3865-3868.

56. S. Grimme, *Journal of Computational Chemistry*, 2006, **27**, 1787.

57. P. Giannozzi, S. Baroni, N. Bonini, M. Calandra, R. Car, C. Cavazzoni, D. Ceresoli, G. L. Chiarotti, M. Cococcioni, I. Dabo, A. Dal Corso, S. de Gironcoli, S. Fabris, G. Fratesi, R. Gebauer, U. Gerstmann, C. Gougoussis, A. Kokalj, M. Lazzeri, L. Martin-Samos, N. Marzari, F. Mauri, R. Mazzarello, S. Paolini, A. Pasquarello, L. Paulatto, C. Sbraccia, S. Scandolo, G. Sclauzero, A. P. Seitsonen, A. Smogunov, P. Umari and R. M. Wentzcovitch, *Journal of physics. Condensed matter : an Institute of Physics journal*, 2009, **21**, 395502.

58. A. Tkatchenko and M. Scheffler, *Physical Review Letters*, 2009, **102**, 073005.

59. V. G. Ruiz, W. Liu and A. Tkatchenko, *Physical Review B*, 2016, **93**, 035118.

60. L. Bellaiche and D. Vanderbilt, *Physical Review B*, 2000, **61**, 7877-7882.

61. K. Reuter and M. Scheffler, *Phys Rev Lett*, 2003, **90**, 046103.

62. K. Reuter and M. Scheffler, *Physical Review B*, 2001, **65**.

63. J. Paier, R. Hirschl, M. Marsman and G. Kresse, *J Chem Phys*, 2005, **122**, 234102.

64. M. Chase Jr, *J. Phys. Chem. Ref. Data, Monograph*, 1998, **9**.

65. R. Włodarczyk, M. Sierka, J. Sauer, D. Löffler, J. J. Uhlrich, X. Yu, B. Yang, I. M. N. Groot, S. Shaikhutdinov and H. J. Freund, *Phys. Rev. B*, 2012, **85**.

66. P. Y. Huang, S. Kurasch, A. Srivastava, V. Skakalova, J. Kotakoski, A. V. Krasheninnikov, R. Hovden, Q. Mao, J. C. Meyer, J. Smet, D. A. Muller and U. Kaiser, *Nano letters*, 2012, **12**, 1081-1086.

67. L. F. Li, H. Tissot, S. Shaikhutdinov and H. J. Freund, *Chemistry of Materials*, 2017, **29**, 931-934.

68. M. F. Brigatti, E. Galan and B. Theng, in *Developments in clay science*, Elsevier, 2013, vol. 5, pp. 21-81.

69. C. Büchner, L. Lichtenstein, M. Heyde and H.-J. Freund, in *Noncontact Atomic Force Microscopy*, Springer, 2015, DOI: 10.1007/978-3-319-15588-3_16, pp. 327-353.

70. T. Engel, *Surface Science Reports*, 1993, **18**, 93-144.

71. G. S. Hutchings and E. I. Altman, *Nanoscale Horiz.*, 2019, **4**, 667-673.

72. H. Tissot, X. F. Weng, P. Schlexer, G. Pacchioni, S. Shaikhutdinov and H. J. Freund, *Surf. Sci.*, 2018, **678**, 118-123.

73. H. W. Klemm, M. J. Prieto, G. Peschel, A. Fuhrich, E. Madej, F. Xiong, D. Menzel, T. Schmidt and H.-J. Freund, *The Journal of Physical Chemistry C*, 2019, **123**, 8228-8243.

74. J. Rumble, *CRC Handbook of Chemistry and Physics*, CRC press, 2017.

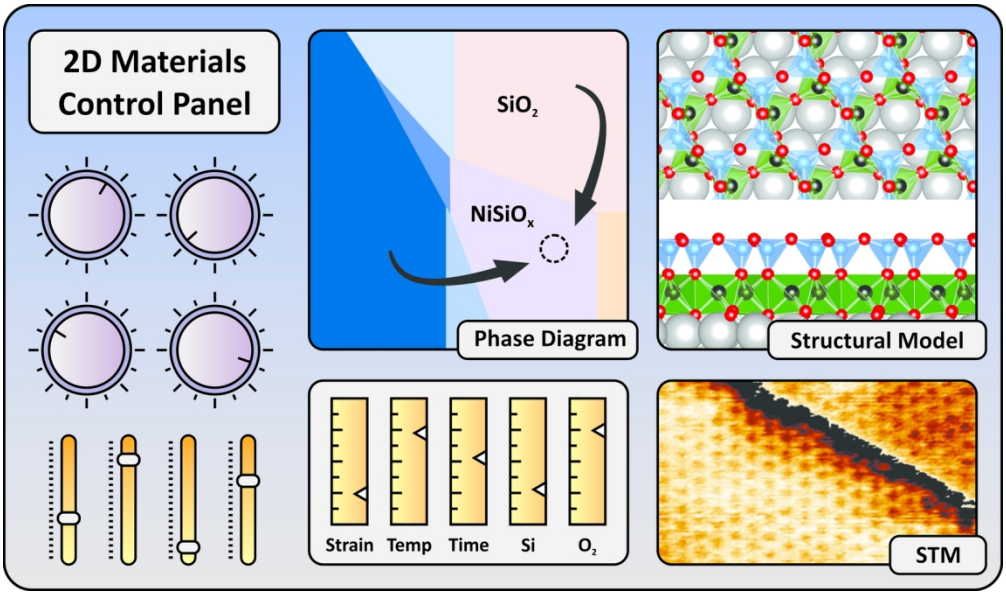

71x41mm (600 x 600 DPI)